Journal of Sound and Vibration (1998) **210**(5), 643–659

DIRECT IDENTIFICATION OF ELASTIC CONSTANTS OF ANISOTROPIC PLATES BY MODAL ANALYSIS: EXPERIMENTAL RESULTS

M. Grédiac†, N. Fournier, P.-A. Paris and Y. Surrel

Département Mécanique et Matériaux, Centre des Matériaux et des Structures, Ecole des Mines, 158, *cours Fauriel*, 42023 *Saint-Etienne Cedex* 2, *France*

(*Received* 25 *April* 1997, *and in final form* 25 *September* 1997)

The determination of the six elastic stiffnesses of thin anisotropic plates from vibration tests is usually performed with numerical procedures based on the finite element or the Rayleigh–Ritz method, which both require assumptions concerning the studied mode shapes. The present paper describes a method based on the measurement and the processing of natural frequencies as well as mode shapes of the vibrating tested plate. As a result, the unknown stiffnesses are determined directly, without any iterative calculations. The experimental aspects of the method are presently described and several results illustrate the relevance of the approach.

1. INTRODUCTION

In part 1 of this study [1], theoretical and numerical aspects of a method allowing the direct determination of flexural stiffnesses of thin composite plates were presented. The main features of this approach were first the fact that natural frequencies and mode shapes of free–free vibrating plates are taken into account, unlike the usual approaches e.g., references [2–8], which only consider natural frequencies. Secondly the fact that the unknown stiffnesses are determined directly, without any iterative calculations. Numerical simulations were carried out and showed that the identification procedure was accurate and not too sensitive to random experimental errors. In the first part of the present paper, the main theoretical aspects of the method are recalled. The experimental set-up is then described and some adaptations of the identification method to the processing of experimental results are discussed. Experimental results carried out on a set of plates are finally presented.

2. BACKGROUND

The following results are directly recalled from the first part of this study [1].

2.1. EQUILIBRIUM OF THE VIBRATING PLATE

The global equilibrium of a uniform free–free plate vibrating in one of its natural modes i is firstly written with the principle of virtual work

† Present address: LERMES-CUST, Université Blaise Pascal, 24, avenue des Landais, BP 206, 63174 Aubière Cedex, France.

0022–460X/98/100643 + 17 $25.00/0/sv971304

$$D_{11}\int_S \frac{\partial^2 W_i}{\partial x^2}\frac{\partial^2 v}{\partial x^2}\,\mathrm{d}S + D_{22}\int_S \frac{\partial^2 W_i}{\partial y^2}\frac{\partial^2 v}{\partial y^2}\,\mathrm{d}S$$

$$+D_{12}\int_S \left(\frac{\partial^2 W_i}{\partial y^2}\frac{\partial^2 v}{\partial x^2}+\frac{\partial^2 W_i}{\partial x^2}\frac{\partial^2 v}{\partial y^2}\right)\mathrm{d}S$$

$$+4D_{66}\int_S \frac{\partial^2 W_i}{\partial x\partial y}\frac{\partial^2 v}{\partial x\partial y}\,\mathrm{d}S$$

$$+2D_{16}\int_S \left(\frac{\partial^2 W_i}{\partial x\partial y}\frac{\partial^2 v}{\partial x^2}+\frac{\partial^2 W_i}{\partial x^2}\frac{\partial^2 v}{\partial x\partial y}\right)\mathrm{d}S$$

$$+2D_{26}\int_S \left(\frac{\partial^2 W_i}{\partial x\partial y}\frac{\partial^2 v}{\partial y^2}+\frac{\partial^2 W_i}{\partial y^2}\frac{\partial^2 v}{\partial x\partial y}\right)\mathrm{d}S$$

$$= -\rho h\omega_i^2\int_S W_i\, v\,\mathrm{d}S, \tag{1}$$

where the D_{ij}'s are the flexural stiffnesses, ω_i is the ith natural frequency, W_i is the corresponding natural mode deflection, h, S and ρ are, respectively, the thickness, the surface area and the specific mass of the plate, and v is the virtual field. The above equation can be written as

$$E_{internal} = E_{inertial}. \tag{2}$$

$E_{internal}$ is the internal virtual work and $E_{inertial}$ is the virtual work done by the inertial forces.

2.2. INTRODUCTION OF SPECIFIC VIRTUAL FIELDS

Assuming that the mode shape W_i and the natural frequency ω_i are measured, one can write a new linear equation of the type of equation (1) for any different virtual field v. However, from a practical point of view, it has been shown in the first part of this study [1], that the best strategy is to consider three modes of vibration: torsion, bending along the x-direction and bending along the y-direction and to associate three independent quadratic virtual fields of the type

$$\begin{cases} v_1(x,y) = x^2 \\ v_2(x,y) = y^2 \\ v_3(x,y) = xy \end{cases}. \tag{3}$$

For the above three quadratic virtual fields, two out of the three partial derivatives required in equation (1) are always zero and the third one is constant. Three terms are therefore zero in equation (1) for each of the virtual fields presented in equation (3). For instance, considering v_1 as the virtual field, equation (1) reduces to

$$2K_{xx}\,D_{11} + 2K_{yy}\,D_{12} + 4K_{xy}\,D_{16} = -\rho h\omega_i^2\int_S W_i\,x^2\,\mathrm{d}S, \tag{4}$$

where only three unknowns are remaining.

For the sake of simplicity, the following notations are introduced. K_{xx}, K_{yy} and K_{xy} are integrals directly proportional to the mean curvature components of the mode shape of the vibrating plate. They are defined by

$$K_{xx} = \int_S \frac{\partial^2 W}{\partial x^2}\,\mathrm{d}S$$

$$K_{yy} = \int_S \frac{\partial^2 W}{\partial y^2}\,\mathrm{d}S. \tag{5}$$

$$K_{xy} = \int_S \frac{\partial^2 W}{\partial x \partial y}\,\mathrm{d}S$$

2.3. DIRECT IDENTIFICATION PROCEDURE

Considering the above three virtual fields and the three modes leads to an overdetermined linear system of nine equations and six unknowns, which is solved using the least-squares method to determine the six stiffnesses.

This system is of the type

$$\mathbf{AD} = \mathbf{B}, \tag{6}$$

where $\mathbf{A}$ is a 9×6 matrix, $\mathbf{D}$ is a 6×1 matrix and $\mathbf{B}$ is a 9×1 matrix. They are defined by

$$\mathbf{A} = 2\left[\begin{array}{cccccc}
K_{xx}^{(t)} & 0 & K_{yy}^{(t)} & 0 & 2K_{xy}^{(t)} & 0 \\
0 & K_{yy}^{(t)} & K_{xx}^{(t)} & 0 & 0 & 2K_{xy}^{(t)} \\
0 & 0 & 0 & 2K_{xy}^{(t)} & K_{xx}^{(t)} & K_{yy}^{(t)} \\
\hline
K_{xx}^{(by)} & 0 & K_{yy}^{(by)} & 0 & 2K_{xy}^{(by)} & 0 \\
0 & K_{yy}^{(by)} & K_{xx}^{(by)} & 0 & 0 & 2K_{xy}^{(by)} \\
0 & 0 & 0 & 2K_{xy}^{(by)} & K_{xx}^{(by)} & K_{yy}^{(by)} \\
\hline
K_{xx}^{(bx)} & 0 & K_{yy}^{(bx)} & 0 & 2K_{xy}^{(bx)} & 0 \\
0 & K_{yy}^{(bx)} & K_{xx}^{(bx)} & 0 & 0 & 2K_{xy}^{(bx)} \\
0 & 0 & 0 & 2K_{xy}^{(bx)} & K_{xx}^{(bx)} & K_{yy}^{(bx)}
\end{array}\right], \tag{7}$$

$$\mathbf{D} = \left[\begin{array}{c} D_{11} \\ D_{22} \\ D_{12} \\ D_{66} \\ D_{16} \\ D_{26} \end{array}\right], \tag{8}$$

$$\mathbf{B} = -\rho h \begin{Bmatrix} \omega_t^2 I_1^{(t)} \\ \omega_t^2 I_2^{(t)} \\ \omega_t^2 I_3^{(t)} \\ \hline \omega_{by}^2 I_1^{(by)} \\ \omega_{by}^2 I_2^{(by)} \\ \omega_{by}^2 I_3^{(by)} \\ \hline \omega_{bx}^2 I_1^{(bx)} \\ \omega_{bx}^2 I_2^{(bx)} \\ \omega_{bx}^2 I_3^{(bx)} \end{Bmatrix}. \tag{9}$$

Subscripts and superscripts t, by and bx denote quantities depending respectively on the twisting mode, the bending mode along the y-direction and the bending mode along the x-direction. $I_i^{(j)}$ are integrals proportional to the virtual work of oriental forces

$$I_i^{(j)} = \int_s W_j(x, y) v_i(x, y)\, \mathrm{d}S; \qquad i = 1, 2, 3; \qquad j = t, by, bx. \tag{10}$$

Numerical simulations carried out in the first part of the study [1] with different types of plates showed the accuracy of the method. It will be shown in section 4 that it is relevant to slightly modify the three fields in equation (3) to simplify the calculation of the virtual work of the inertial forces. This is due to the fact that the deflection fields W_j are not directly provided by the optical set-up used in the present work as slope fields are effectively measured. Let us now examine the practical experimental aspects of the procedure.

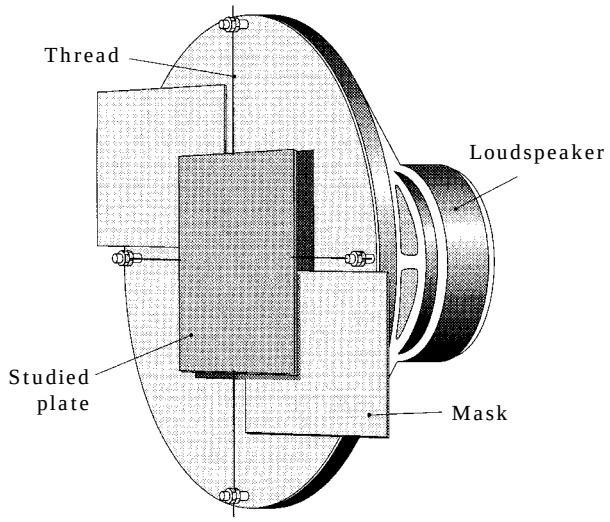

Figure 1. Fixation of the tested plate and mask for the twisting mode.

3. EXPERIMENTAL SET-UP

3.1. EXCITATION OF THE SPECIMEN AND MEASUREMENT OF THE NATURAL FREQUENCIES

Figure 1 shows the tested specimen which is suspended by four very thin threads fixed near the nodal lines of the mode shape to be measured. Hence, free–free boundary conditions are obtained. The excitation technique is obtained with a loudspeaker located near the specimen. Non-contact devices allowing the measurement of the natural frequencies are not available in the laboratory and a Bruel & Kjaër type 4374 accelerometer is used. It is located at one of the corners of the plate for the twisting mode and at the center of the plate for the two last modes (see Figures 5–7). The deflection is maximum at these points. Hence, the sensitivity will be optimum for the measurement of acceleration. Note that the mass of the accelerometer is not negligible compared to the mass of the tested plates. It has therefore a significant influence on the mode shapes of the tested plates. This influence will be taken into account later in the identification procedure. Natural frequencies are determined by frequency sweeping. The sine signal is provided by the generator of a Bruel & Kjaër multi-channel analysis system 3550 through an audio-amplifier. The acceleration signal of the tested specimen is analyzed by the system and the first natural frequencies are detected.

As explained previously, three mode shapes must be measured. An optical set-up described in the next section is used. During the measurement of the mode, the frequency of the loudspeaker is adjusted to the studied natural frequency and the acoustic waves force the specimen to vibrate in the corresponding mode shape. Note that the magnitude of the deflection must be high enough to be measurable. Hence, a "mask" is interposed between the loudspeaker and the plate to increase the efficiency of the loudspeaker. The shape of the mask obviously depends on the shape of the mode to be measured. The mask designed for the twisting mode is depicted in Figure 1.

3.2. OPTICAL SET-UP

Many optical techniques providing mode shapes are available in the literature. Most of them are based on the principle of holography or speckle. To the knowledge of the authors, only qualitative information is often extracted from those measurements. The present approach, however, requires quantitative information, as integrals in equation (1) directly involve curvatures and deflections. A specific optical set-up has therefore been developed. The principle is based on deflectometry, not in the form of the moiré deflectometry used by Kafri *et al*. [9, 10, 11], but in the simpler set-up of the phase-stepped Ronchi test [12, 13]. It is simpler than other shearing interferometry set-ups [14], and allows easy phase-shifting, which is a current method to improve the accuracy of optical setups. Precise measurement of the local slopes of the surface under investigation can be done and only one differentiation has to be done in order to obtain curvatures, and one integration to obtain deflections.

The principle is sketched in Figure 2. The optical method relies on specular reflection from the plate. Hence the plate is coated with a very thin layer of epoxy resin. It is then illuminated by a collimated beam obtained from a light point source (LS) located at the focus of the fields lens (FL). After reflection, all rays having the same direction (e.g., rays reflected at points A and B) converge at the same point ξ, η of the focal plane of the lens FL, with:

$$\xi = 2f\frac{\partial w}{\partial x}, \qquad \eta = 2f\frac{\partial w}{\partial y}, \tag{11}$$

where w is the deflection.

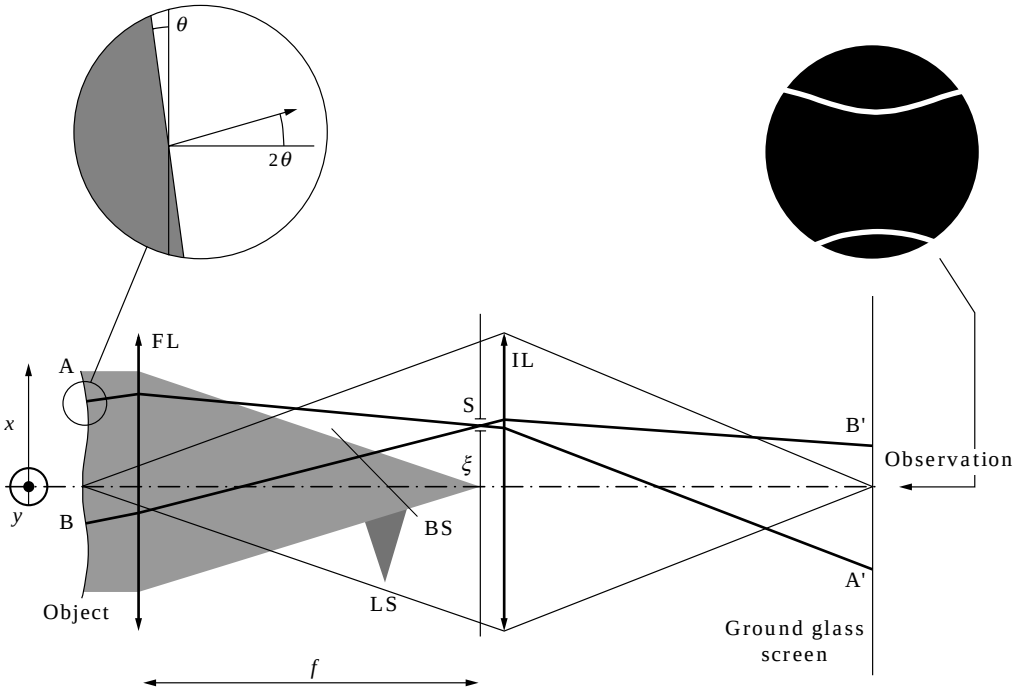

Figure 2. Schematic of the deflectometric set-up, using a filtering slit. A slope contour is seen on the screen. BS: beamsplitter; FL: field lens; IL: imaging lens; S: filtering source; LS: light source.

If a vertical slit S (i.e., aligned with the η-axis) is placed at this point, the light coming from points where the local x-slope is different is blocked. In this case, the image of the plate made by the imaging lens (IL) only receives light from points with the same x-slope. So, x-slope contours are observed. If a horizontal slit is used, y-slope contours are observed. In order to have more information at once, the slit can be replaced by an array of slits, that is a grid, as indicated in Figure 3. In the following, the grid is supposed to have its lines oriented parallel to the η-axis, so that x-slopes are measured. The obtained slope contour pattern looks very similar to classical interference fringes, apart from the fact that they are much more stable. Indeed, low frequency vibrations induce mainly rigid body translations which do not change slopes. The present set-up can be used to realize static or dynamic measurements. In this last case, a chopper is added in front of the light source to freeze the motion of the vibrating plate. The synchronization between the chopper and the vibrating device is tuned to record the image of the plate at the maximum deflection. Full details concerning the characteristics of this optical set-up can be found in references [15, 16].

4. CALCULATION OF THE INTEGRALS

4.1. INTERNAL VIRTUAL WORK

As may be seen in the basic equation (1), the coefficient of each unknown D_{ij} is directly obtained from integrals involving the average curvatures of the three considered mode shapes. From a practical point of view, each measured slope pattern of the mode shape provides two curvature patterns by numerical differentiation. The mean value of each curvature field is then computed. Note that the two cross derivatives $\partial^2 w/\partial x \partial y$ and

$\partial^2 w/\partial y \partial x$ are theoretically equal. This property is used to check the consistency of two sets of slope fields obtained in two orthogonal directions.

4.2. VIRTUAL WORK OF THE INERTIAL FORCES

The integrals $I_i^{(j)}$ defined in equation (10) directly involve the deflection W_j corresponding to the mode j. The experimental data are however presently the two slopes, i.e., the two partial derivatives of the deflection in two orthogonal directions. A relevant strategy has therefore to be found to determine these integrals from slopes. This problem did not appear in the first part of the study [1], as the finite element program used for the simulations directly provided the deflections corresponding to a given mode. In the present experimental part, the following method has been used.

Consider that the shape of the tested plate is a $2a \times 2b$ rectangle and let us expand the deflection with Legendre polynomials. Such polynomials are chosen because of their orthogonality property on such surfaces.

$$W(x, y) = \sum_{i=0}^{\infty} \sum_{j=0}^{\infty} A_{ij} \, \mathrm{P}_i\left(\frac{x}{a}\right) \mathrm{P}_j\left(\frac{y}{b}\right). \tag{12}$$

x and y are divided respectively by a and b because the orthogonality property of Legendre polynomials is valid over $[-1, 1]$. Denoting u a variable lying between -1 and 1, the orthogonality property can be written as

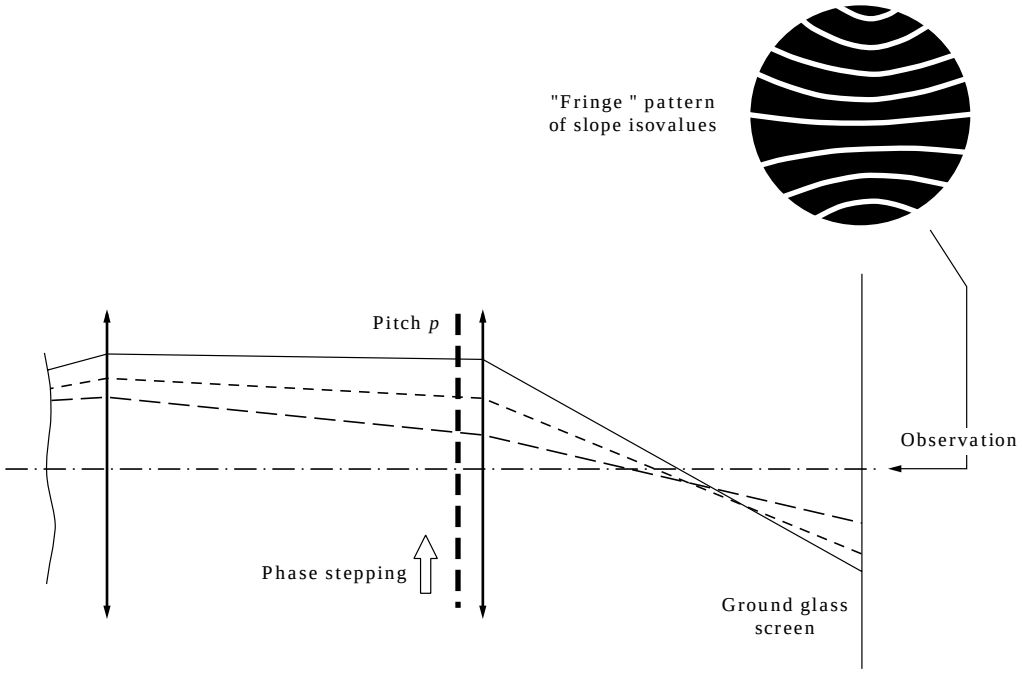

Figure 3. Deflectometric set-up using a filtering grid. Slope contours looking like a fringe pattern are imaged onto the screen.

$$\begin{cases} \displaystyle\int_{-1}^{1} \mathrm{P}_i(u)\mathrm{P}_j(u)\,\mathrm{d}u = 0 & \text{if } i \neq j \\ \displaystyle\int_{-1}^{1} \mathrm{P}_i^2(u)\,\mathrm{d}u = \frac{2}{2i+1} \end{cases}, \tag{13}$$

and the first four Legendre polynomials are

$$\begin{cases} \mathrm{P}_0(u) = 1 \\ \mathrm{P}_1(u) = u \\ \mathrm{P}_2(u) = \frac{3}{2}u^2 - \frac{1}{2} \\ \mathrm{P}_3(u) = \frac{5}{2}u^3 - \frac{3}{2}u \end{cases} \tag{14}$$

Introducing equation (12) in the definition of I given in equation (10), I becomes

$$I = \int_{-a}^{a}\int_{-b}^{b} \sum_{i=0}^{\infty}\sum_{j=0}^{\infty} A_{ij}\,\mathrm{P}_i\left(\frac{x}{a}\right)\mathrm{P}_j\left(\frac{y}{b}\right)v(x,y)\,\mathrm{d}x\,\mathrm{d}y. \tag{15}$$

Remembering now that the three virtual fields leading to average curvatures in equation (1) are quadratic, one can choose advantageously the three following fields instead of v_1, v_2 and v_3 given in equation (3). These new fields are directly products of Legendre polynomials.

$$\begin{cases} v_1'(x,y) = \frac{2}{3}\,\mathrm{P}_2\left(\frac{x}{a}\right)\mathrm{P}_0\left(\frac{y}{b}\right) = v_1\left(\frac{x}{a},\frac{y}{b}\right) - \frac{1}{3} \\ v_2'(x,y) = \frac{2}{3}\,\mathrm{P}_0\left(\frac{x}{a}\right)\mathrm{P}_2\left(\frac{y}{b}\right) = v_2\left(\frac{x}{a},\frac{y}{b}\right) - \frac{1}{3}. \\ v_3'(x,y) = \mathrm{P}_1\left(\frac{x}{a}\right)\mathrm{P}_1\left(\frac{y}{b}\right) = v_3\left(\frac{x}{a},\frac{y}{b}\right) \end{cases} \tag{16}$$

There are two differences between the above fields and the fields recalled in equation (3). First, a constant term $-\frac{1}{3}$ has been presently added to v_1 and v_2. From a mechanical point of view, this constant term introduces a constant virtual deflection which has no influence as the plate is in equilibrium. Second, x and y are divided by a and b respectively to gain the benefit of the orthogonality property of the Legendre polynomials. As a result, second derivatives in equation (1) are also divided by the same quantity and the linear system is finally not modified. Considering the above virtual fields as products of Legendre polynomials significantly simplifies equation (15). For example, with $v = v_1$, I becomes I_1

$$I_1 = \int_{-a}^{a}\int_{-b}^{b} \sum_{i=0}^{\infty}\sum_{j=0}^{\infty} A_{ij}\,\mathrm{P}_i\left(\frac{x}{a}\right)\mathrm{P}_j\left(\frac{y}{b}\right)\frac{2}{3}\,\mathrm{P}_2\left(\frac{x}{a}\right)\mathrm{P}_0\left(\frac{y}{b}\right)\mathrm{d}x\,\mathrm{d}y. \tag{17}$$

Introducing now the orthogonality property, I_1 can be written as

$$I_1 = \frac{2}{3} \times \frac{2}{2\times 2+1} \times \frac{2}{2\times 0+1}\,A_{20} \times \frac{1}{ab}. \tag{18}$$

Finally

$$I_1 = \tfrac{8}{15} A_{20} \times \frac{1}{ab}. \tag{19}$$

In the same way, denoting I_2 and I_3 the integrals corresponding to v_2' and v_3' respectively

$$\begin{cases} I_2 = \tfrac{8}{15} A_{02} \times \dfrac{1}{ab} \\ I_3 = \tfrac{4}{9} A_{11} \times \dfrac{1}{ab} \end{cases}. \tag{20}$$

So, only three coefficients of the Legendre polynomial expansion of $W(x, y)$ are necessary to compute the virtual work of the inertial forces for a rectangular plate.

The last point is to retrieve these coefficients from slope fields which constitute the experimental data provided by the optical set-up. It can be shown [17] using the orthogonality property of the Legendre polynomials that the A_{ij} coefficients in equation (12) can easily be computed from slope fields by two different ways when $ij \neq 0$

$$\begin{cases} A_{ij} = \dfrac{2i+1}{4} \displaystyle\int_{-a}^{a}\int_{-b}^{b} \frac{\partial W}{\partial x}\left(\mathrm{P}_{i-1}\left(\frac{x}{a}\right) - \mathrm{P}_{i+1}\left(\frac{x}{a}\right)\right)\mathrm{P}_j\left(\frac{y}{b}\right) \mathrm{d}x\, \mathrm{d}y \qquad \forall i \geqslant 1, \qquad \forall j \geqslant 0 \\ \text{or} \\ A_{ij} = \dfrac{2j+1}{4} \displaystyle\int_{-a}^{a}\int_{-b}^{b} \frac{\partial W}{\partial y}\left(\mathrm{P}_{j-1}\left(\frac{y}{b}\right) - \mathrm{P}_{j+1}\left(\frac{y}{b}\right)\right)\mathrm{P}_i\left(\frac{x}{a}\right) \mathrm{d}x\, \mathrm{d}y \qquad \forall i \geqslant 0, \qquad \forall j \geqslant 1. \end{cases} \tag{21}$$

Hence, A_{20} and A_{02} can be retrieved from one slope field only while A_{11} can be retrieved from both fields. This property can be used to assess the consistency of the measurements. From a practical point of view, the average of those two values is considered in the calculations. Note finally that using the present approach avoids the determination of coefficient A_{00}, which is the constant of integration required to obtain the deflection from the slopes.

4.3. CONTRIBUTION OF THE ACCELEROMETER TO THE VIRTUAL WORK OF INERTIAL FORCES

Equation (1) has been written for a free–free plate only. As an accelerometer has been used in the experiments to measure the frequencies, the contribution of an additional mass has to be taken into account in this equation. This can be done easily by adding to the right-hand side in equation (1) the virtual work of inertial forces due to the accelerometer. This quantity, called correcting term due to the accelerometer, is denoted $E_{accelerometer}$ in the following

$$E_{accelerometer} = M_{acc}\, \gamma_{acc}\, v_i'\,(x_{acc}, y_{acc}), \tag{22}$$

where M_{acc} is the mass of the accelerometer, γ_{acc} is the acceleration measured by the accelerometer, x_{acc}, y_{acc} are the co-ordinates of the accelerometer and $v_i'\,(x_{acc}, y_{acc})$ is the value of the virtual field at the location of the accelerometer. This value is given for each mode and each virtual field in Table 1. As a result, equation (2) becomes

$$E_{internal} = E_{inertial} + E_{accelerometer}, \tag{23}$$

and a matrix **C** has to be added in system (6)

TABLE 1

Value of the virtual field at the location of the accelerometer

Vibration mode	x_{acc}	y_{acc}	Virtual field	Value of the virtual field
Torsion	a	b	v_1'	$\frac{2}{3}$
			v_2'	$\frac{2}{3}$
			v_3'	1
Bending, y direction	0	0	v_1'	$-\frac{1}{3}$
			v_2'	$-\frac{1}{3}$
			v_3'	0
Bending, x direction	0	0	v_1'	$-\frac{1}{3}$
			v_2'	$-\frac{1}{3}$
			v_3'	0

$$\mathbf{AD} = \mathbf{B} + \mathbf{C}, \tag{24}$$

where $\mathbf{C}$ is a 9×1 matrix whose components are the nine correcting terms obtained with combinations of the three deflections and the value of the three virtual fields at the location of the accelerometer, as given in Table 1.

$$\mathbf{C} = -M_{acc} \begin{pmatrix} \frac{2}{3}\gamma_{acc}^{(t)} \\ \frac{2}{3}\gamma_{acc}^{(t)} \\ \gamma_{acc}^{(t)} \\ \hline -\frac{1}{3}\gamma_{acc}^{(by)} \\ -\frac{1}{3}\gamma_{acc}^{(by)} \\ 0 \\ \hline -\frac{1}{3}\gamma_{acc}^{(bx)} \\ -\frac{1}{3}\gamma_{acc}^{(bx)} \\ 0 \end{pmatrix}. \tag{25}$$

The influence of the correcting term also depends on the mass of the accelerometer with respect to the mass of the tested plate. To give an idea of the influence of this term to the identified stiffnesses, a finite element simulation has been performed with the ANSYS 5.2 package. The $100 \times 100 \times 1$ mm^3 unidirectional tested plate is in graphite/epoxy. Its mass is 15 g. The accelerometer is modelled as a point mass of 0·7 g located at a corner of the plate for the twisting mode and at the center of the plate for the two last bending modes. The plate is meshed with 60×60 Shell 63 quadratic elements. The identification procedure is applied as in the first part of the study [1] with and without taking into account the accelerometer to observe its influence. Results are collected in Table 2. As may be seen, some severe errors appear when the correcting term is not taken into account. D_{12}, which is known to be the most sensitive term (see e.g., reference [8]), becomes negative, which is unrealistic. On the other hand, identified values are very close to the actual ones when that term is considered. As a result, this correction is always done in the experiments described below.

4.3.1. *Conclusion*

In conclusion, the system obtained in the first part of the study [1] is slightly modified to consider some specificities of the experimental set-up: the virtual work produced by the inertial forces is directly computed from the slope field provided by the optical set-up and the influence of the accelerometer is taken into account. As a result, a set of nine linear equations is obtained. In the following, this system is solved using the least-square method to obtain the six unknown stiffnesses. Results will be given in terms of normalized stiffnesses homogeneous to moduli and defined by

$$D_{ij}^{*} = \frac{12}{h^3} D_{ij}. \tag{26}$$

5. RESULTS AND DISCUSSION

5.1. TESTED PLATES

Three composite plates have been investigated in the present study. The constitutive material is a graphite/epoxy, whose elastic coefficients are respectively $E_x = 124{\cdot}9$ GPa, $E_y = 9{\cdot}05$ GPa, $G_{xy} = 4{\cdot}96$ GPa and $v_{xy} = 0{\cdot}34$. These constants have been measured with standard tests described in reference [18]. The stacking sequences are respectively $[0_4]_s$, $[0, 90]_{2s}$ and $[0, 45, 90, 135]_s$. The thickness of the three plates is 1 mm and their specific mass is 1510 kg/m^3. The flexural stiffnesses are estimated using the classical theory of laminated plates and will be compared in the following to the values obtained from experiments. They are reported in the first row of Tables 4–6. The plates have a square 100×100 mm planform. They are coated before testing with a layer of reflective epoxy resin which is obtained by pressing the plate and the resin between two glass plates. This layer is very thin (less than

TABLE 2

Identified normalized stiffnesses with and without the correcting term for the unidirectional graphite/epoxy plate

	D_{11}^{*} (GPa)	D_{22}^{*} (GPa)	D_{12}^{*} (GPa)	D_{66}^{*} (GPa)	D_{16}^{*} (GPa)	D_{26}^{*} (GPa)
Actual value	125·00	9·12	3·10	4·96	0	0
Calculated value without correcting term	119·81	9·85	−1·40	3·91	−0·06	−0·54
Calculated value with correcting term	129·83	9·25	2·97	5·02	0·13	0·05

TABLE 3

Consistency of two measurements performed in two orthogonal directions. Comparison between the mean value of $\overline{\varepsilon_{xy}}$ and $\overline{\varepsilon_{yx}}$ on the top surface of the vibrating plate

γ_{acc} (m/s^2)	$\overline{\varepsilon_{xy}}$ (10^{-6})	$\overline{\varepsilon_{yx}}$ (10^{-6})	Difference (10^{-6})
22·3	0·32	0·39	0·07
26·6	0·41	0·45	0·04
39·5	0·72	0·71	0·01
56·5	1·07	1·07	0·00
65·6	1·25	1·22	0·03

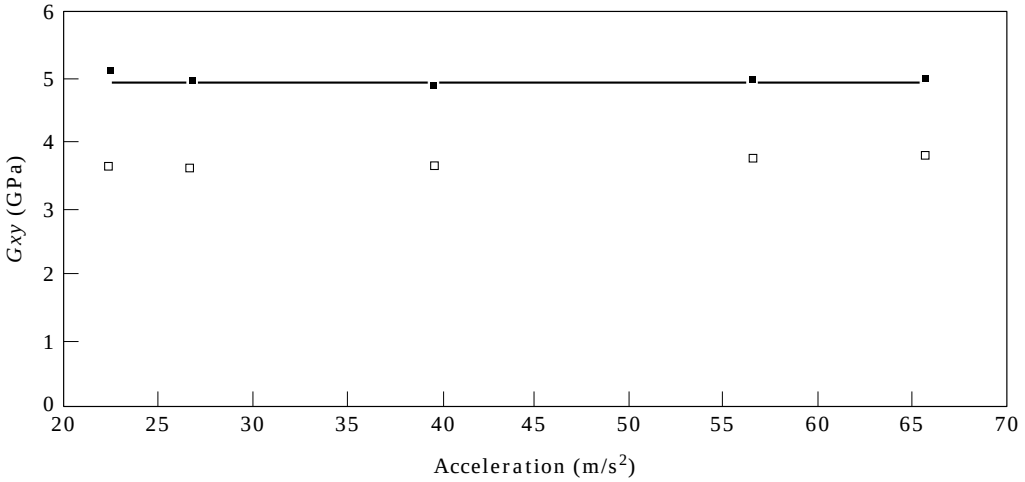

Figure 4. Shear modulus of the unidirectional plate for various excitation levels. ■, With correcting term; □, without correcting term; —, Iosipescu (after Pierron and Vautrin [18]).

10^{-2} mm) and it has been checked that its influence on the measured stiffnesses is negligible.

5.2. PRELIMINARY TESTS

5.2.1. *Introduction*

Some preliminary twisting tests have been performed to verify first the consistency of two sets of results obtained along both x and y directions and second to examine the independence of the results on the magnitude of the excitation. To simplify the procedure, the first plate described above, whose sides are parallel to the directions of orthotropy, is tested and it is assumed that the average curvatures along both x and y directions are zero. Hence, in the present section

$$K_{xx}^{(t)} = 0, \qquad K_{yy}^{(t)} = 0. \tag{27}$$

5.2.2. *Consistency of the experimental results*

As explained above, $K_{xy}^{(t)}$ can be calculated either with the $\partial w/\partial x$ or the $\partial w/\partial y$ slope pattern and the results are expected to be equal. Both of them have been computed in the present experiment and compared. Results given in terms of average surface strain components are collected in Table 3. The average surface strain components ϵ_{xy} and ϵ_{yx} are obtained by multiplying respectively $K_{xy}^{(t)}$ and $K_{yx}^{(t)}$ by $-h/2S$. As may be seen, both sets of results are very close: the difference is less than $0{\cdot}07 \times 10^{-6}$ and it tends to decrease as the acceleration increases. In that case, the two sets of measurements performed in two orthogonal directions are consistent. In the following, $K_{xy}^{(t)}$ will therefore be the average of the calculations performed in both x and y directions.

5.2.3. *Linearity of the response*

The non-linearity of the shear properties of composite materials is often described when quasi-static tests are carried out at higher strain levels than in dynamics (e.g., reference [19]). As the above method is based on the assumption that the tested plates are elastic, it must be checked that the shear modulus does not depend on the magnitude of the load, i.e., on the magnitude of the vibration in the present case. When the excitation produced

by the loudspeaker increases, the acceleration measured by the accelerometer and the stress and strain levels increase in the plate and so it can be checked that the shear stiffness remains constant.

As $K_{xx}^{(t)}$ and $K_{yy}^{(t)}$ have been assumed to be zero in the above section, the third equation in system (24) only involves D_{66}. Hence this term can be determined directly

$$D_{66} = -\frac{1}{2K_{xy}^{(t)}}\,\omega_t^2\,(\rho h I_3^{(t)} + M_{acc}\,a^2). \tag{28}$$

The normalized shear stiffness D_{66}^* is computed for different excitation levels using the above equation. It is expected to be equal to the in-plane shear modulus as the plate is unidirectional. Results obtained at different levels are plotted in Figure 4. As may be seen, this stiffness remains independent of the stress level. It is also very close to the static value measured on the same material with a standard Iosipescu shear test [18]. Finally, the influence of the correcting term can be assessed in the present case, as the D_{66}^* term determined without that term has also been reported in the same figure. It can be seen that ignoring that term leads to a severe error.

5.2.4. *Example of slope patterns*

Examples of slope fields measured on the unidirectional plate are given in Figures 5–7. For the twisting mode, it is clear that slopes in the x direction mainly depend on y. In the same way, slopes in the y direction mainly depend on x. For that mode, the xy term would obviously be predominant in the expansion of the mode shape using the Rayleigh–Ritz method. Note however that fringes are slightly inclined in the second pattern. It has been checked with a finite element simulation that it is due to the accelerometer. The bending mode along the y direction is depicted in Figure 6. As may be seen, the curvature in the y direction is predominant, while the curvature along the x

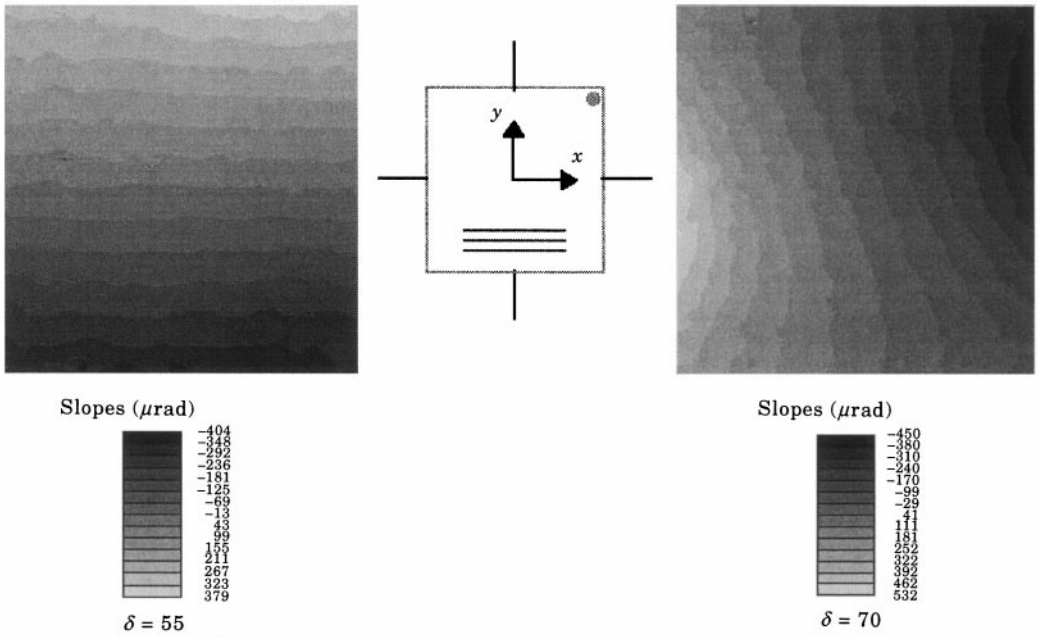

Figure 5. Twisting mode, $f = 169$ Hz, measured slope patterns in the x and y directions. —, Threads; ●, accelerometer; ≡, direction of the fibers.

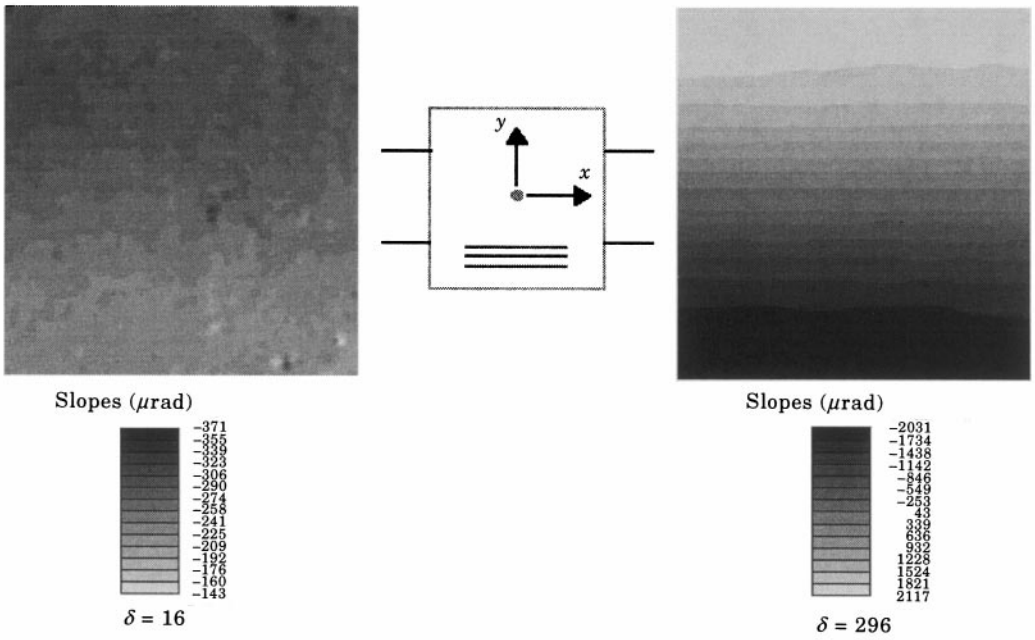

Figure 6. Bending in the y direction, $f = 244$ Hz, measured slope patterns in the x and y directions. —, Threads; ●, accelerometer; ≡, direction of the fibers.

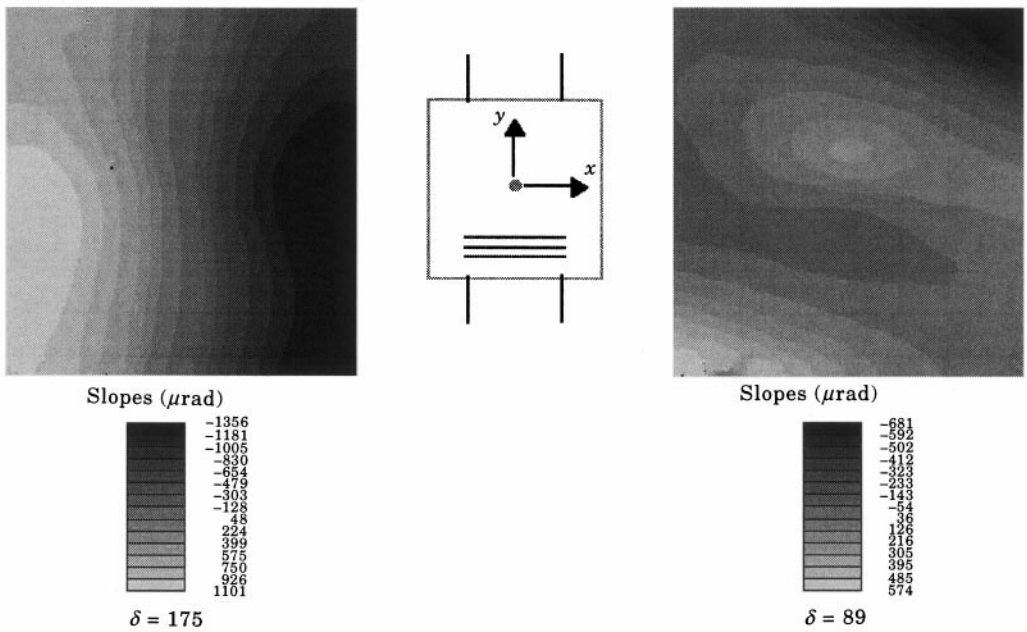

Figure 7. Bending in the x direction, $f = 876$ Hz, measured slope patterns in the x and y directions. —, Threads; ●, accelerometer; ≡, direction of the fibers.

direction is very small. This is mainly due to the fact that the minor Poisson's ratio, which directly governs the ratio between curvatures along the x and y directions, is very small for such an orthotropic plate. The bending along the x direction is finally illustrated in Figure 7. In that direction, the major Poisson's ratio is involved and the curvature in the y direction is therefore higher. Note that the order of magnitude of the slopes for the three mode shapes remains less than 2×10^{-3} rad. The order of magnitude of the maximum deflection is about some tens of μm for the three modes.

5.3. RESULTS

The values obtained with the above procedure applied to the three laminated plates described in section 5.1 are collected in Tables 4–6 and compared to the so-called expected ones, which are calculated with the classical lamination theory. As a general remark, a good agreement between expected and identified values can be observed. The difference between both sets of results depends on the stacking sequence as well as on the stiffness itself. The highest difference is generally obtained for D_{12}^*, which is directly related to the Poisson's effect. This result is in good agreement with the conclusions of numerical simulations carried out in the first part of this study [1]. They showed that this parameter was the most sensitive to measurement errors. This property is certainly due to its small contribution to the mode shapes. This point has already been noted by different authors (see e.g., reference [8]). In the same way, the shear coupling stiffness D_{16}^* presents a high

TABLE 4

Normalized stiffnesses computed with the classical lamination theory compared with the identified corresponding ones, unidirectional graphite/epoxy plate

	D_{11}^*	D_{22}^*	D_{12}^*	D_{66}^*	D_{16}^*	D_{26}^*
Expected (GPa)	124·90	9·12	3·10	4·96	0	0
Identified (GPa)	121·14	9·82	2·08	5·49	−2·09	−0·13
Difference (%)	−3·0	7·7	−32·9	10·7	—	—

TABLE 5

Normalized stiffnesses computed with the classical lamination theory compared with the identified corresponding ones, $[0, 90]_{2s}$ *graphite/epoxy plate*

	D_{11}^*	D_{22}^*	D_{12}^*	D_{66}^*	D_{16}^*	D_{26}^*
Expected (GPa)	89·40	45·60	3·10	4·96	0	0
Identified (GPa)	89·83	47·83	4·24	5·07	−1·92	−0·47
Difference (%)	0·5	4·9	36·7	2·2	—	—

TABLE 6

Normalized stiffnesses computed with the classical lamination theory compared with the identified corresponding ones, $[0, 45, 90, 135]_s$ *graphite/epoxy plate*

	D_{11}^*	D_{22}^*	D_{12}^*	D_{66}^*	D_{16}^*	D_{26}^*
Expected (GPa)	86·40	31·60	11·60	13·40	8·21	8·21
Identified (GPa)	85·99	29·26	7·16	13·48	8·79	10·33
Difference (%)	−0·5	−7·4	−38·2	0·6	7·1	25·8

difference between expected and identified values for the last plate. This is probably due to the same reason as above. D_{66}^*, D_{22}^* and D_{11}^* are obtained with the highest accuracy, as their influence is prevailing in the first, second and third modes respectively. For the first plate, it must be noted that the identified value of D_{66}^* is different from the value obtained in the above section (5·5 GPa instead of 5·0 GPa), when the coupling stiffnesses are assumed to be zero. It seems that the extra freedom introduced by non-zero values of D_{16}^* and D_{26}^* influence the identified value of D_{66}^*, as they are involved in the same equations in system (24). Note however that the presently so-called expected values are in fact computed with the classical lamination theory. Hence, eventual discrepancies due to the manufacturing or to the misalignement of the fibers are not taken into account. As a result, the assumption of zero values for D_{16}^* and D_{26}^* is probably not rigorously verified in the present case.

6. CONCLUSION

A solution of the inverse problem of determining elastic constants of anisotropic plates from whole-field slope measurements is presented in this paper. Three modes involving the whole set of unknowns are considered. The main feature of the present approach is to take into account measured values of natural frequencies as well as measured mode shapes. Then, no assumption is made concerning the mode shape contrarily to most of the methods found in the literature which are based on the Rayleigh–Ritz or finite element methods. From a numerical point of view, the main advantage is that the stiffnesses are determined directly. Experimental results obtained on a set of three different anisotropic plates show the robustness of the method.

REFERENCES

1. M. Grédiac and P.-A. Paris 1996 *Journal of Sound and Vibration* **195**, 401–415. Direct identification of elastic constants of anisotropic plates by modal analysis: theoretical and numerical aspects.
2. E. O. Ayorinde and R. F. Gibson 1993 *Composites Engineering* **3**, 395–407. Elastic constants of orthotropic composite materials using plate resonance frequencies, classical lamination theory and an optimized three-mode Rayleigh formulation.
3. L. R. Deobald and R. F. Gibson 1988 *Journal of Sound and Vibration* **124**, 269–283. Determination of elastic constants of orthotropic plates by a modal analysis/Rayleigh–Ritz technique.
4. K.-E. Fällström 1991 *Polymer Composites* **12**, 306–314. Determining material properties in anisotropic plates using Rayleigh's method.
5. P. S. Frederiksen 1995 *Report No*. 500 *of the Danish Center for Applied Mathematics and Mechanics*, *Technical University of Denmark*. Identification of elastic constants including transverse shear moduli of thin orthotropic plates.
6. M. E. McIntyre and J. Woodhouse 1988 *Acta Metallurgica* **36**, 1397–1416. On measuring the elastic and damping constants of orthotropic sheet materials.
7. C. M. Mota Soares, M. Moreira de Freitas, A. L. Araújo and P. Pedersen 1993 *Composite Structures* **25**, 277–285. Identification of material properties of composite plate specimens.
8. H. Sol 1986 *Doctoral dissertation*, *University of Brussels*. Identification of anisotropic plate rigidities using free vibration data.
9. O. Kafri and K. Kreske 1988 *Applied Optics* **27**, 878–882.
10. O. Kafri and L. Glatt 1988 *Applied Optics* **27**, 351–353. High-sensitivity reflection-transmission moiré deflectometer.
11. O. Kafri, E. Keren, K. Kreske and Y. Zac 1990 *Applied Optics* **29**, 133–136. Moiré deflectometry with a focus beam: radius of curvature, microscopy and thickness analysis.
12. W. Omura and T. Yatagai 1988 *Applied Optics* **27**, 523–528. Phase measuring Ronchi test.
13. D. Malacara 1990 *Applied Optics* **29**, 3633–3637. Analysis of the interferometric Ronchi test.

14. A. Assa, J. Politch and A. A. Bester 1979 *Experimental Mechanics* **19**, 129–137. Slope and curvature measurement by a double-frequency-grating shearing interferometer.
15. N. Fournier, M. Grédiac, P.-A. Paris and Y. Surrel 1997 Submitted *to Experimental Mechanics*. Phase-stepped deflectometry applied to shape measurement of bent plates.
16. N. Fournier, M. Grédiac, P.-A. Paris and Y. Surrel 1997 *Proceedings of the International Conference on Materials and Mechanics* '97, *Tokyo*. pp. 101–106, published by M. Nakamura. Measurement of plate eigenmodes by deflectometry.
17. M. Grédiac 1997 *Applied Optics*. **36,** 4823–4829. pp 101–106. A method for surface reconstruction from slope or curvature measurements on rectangular areas.
18. F. Pierron and A. Vautrin 1994 *Composite Science and Technology* **52**, 61–72. Accurate comparative determination of the in-plane shear modulus of 300/914 by the Iosipescu and 45 off-axis tests.
19. Y. Surrel and A. Vautrin 1993 *Composite Science and Technology* **49**, 45–50. Plastic behaviour of fibrous laminae.